Mechanics Research Communications 129 (2023) 104098

Contents lists available at ScienceDirect

Mechanics Research Communications

journal homepage: www.elsevier.com/locate/mechrescom

Characterization and modeling of the anisotropic behavior of the porcine dermis

Suman Jaiswal [a], Taisiya Sigaeva [b], Siva P.V. Nadimpalli [c], Samuel Lieber [d], Shawn A. Chester [a,*]

[a] Department of Mechanical Engineering, New Jersey Institute of Technology, Newark, NJ 07102, USA
[b] Department of Systems Design Engineering, University of Waterloo, ON N2L 3G1, Canada
[c] Department of Mechanical Engineering, Michigan State University, East Lansing, MI, 48824, USA
[d] School of Applied Engineering and Technology, New Jersey Institute of Technology, Newark, NJ 07102, USA

ARTICLE INFO

Keywords:
Anisotropic
Porcine
Dermis
Non-symmetric
Constitutive

ABSTRACT

This work uses a combined experimental and modeling investigation into the anisotropic behavior of porcine dermis. Porcine skin tissues have been used in various medical, cosmetic, and biomedical research applications. However, their tensile behavior still needs to be fully characterized. Much of the existing work uses the uniaxial experimental data from two orthogonally oriented specimens to inform and model the anisotropic behavior of the tissue. However, the skin has a complex fibrous architecture with several non-symmetric fiber families. Accordingly, we have (i) mechanically characterized the behavior of the porcine dermis using the experimental data from three differently orientated uniaxial tensile specimens (two orthogonal and one diagonal) and (ii) developed an enhanced constitutive model to better capture the observed behavior from three different orientations. The enhanced model takes into account the non-symmetric planar fiber distribution, the non-linearity of the ground substance, as well as the varying fiber responses along three orientations. We demonstrate significant improvement of the enhanced model over the prior literature to capture the observed nonlinear and anisotropic behavior from three differently oriented specimens simultaneously.

1. Introduction

The mechanical behavior of skin has importance for various fields such as cosmetic products [1], clinical and biomedical applications [2–4]. Specifically, skin tissues are excellent candidate materials as meshes for hernia repair [5] and breast reconstruction surgery [6]. A thorough understanding of the mechanical behavior of skin tissues would improve the performance of various existing bio-medical devices or even aid in the development of new and improved devices. However, the mechanical behavior of skin is complex and requires robust mechanical characterization and advanced constitutive modeling.

Skin tissues are known to be multi-layered fiber-reinforced composite materials. In many applications, the dermis is the mechanically relevant layer consisting of collagen fibers embedded in a gel-like matrix called the ground substance [7,8]. It is well established in the literature that the structural arrangement of collagen fibers impacts the mechanical response of the tissues [9–13]. In the undeformed configuration, these fibers are in a crimped state and become uncoiled under tensile load. Further, in uniaxial tests, they tend to re-align in the direction of loading [14]. Skin tissues exhibit non-linear and anisotropic behavior due to the underlying fiber distribution and cross-linking coupled with the uncoiling and subsequent engagement of the collagen fibers with deformation [8,11].

Numerous contributions in the literature have experimentally explored the non-linear and anisotropic mechanical behavior of various skin tissues. Several seminal contributions have been reported that are related to human skin [12,15–18], bovine skin [19,20], rat skin [21], and porcine skin [22–25]. In most cases, specifically for porcine skin, uniaxial experiments have been performed in only two orthogonal directions, particularly the spine direction and perpendicular to spine direction [22,24–27], therefore not fully capturing the response along the diagonal direction, which may be the natural direction for load-bearing fiber families *in vivo*. Further, the microstructural details of fiber distribution, specifically in the plane of the dermis, were not considered [7,12,22,24,25]. The recent work of Jaiswal et al. [28] experimentally characterized the collagen fiber distribution in the plane of the porcine dermis and concluded that, generally, it is non-symmetric. These details are yet to be accounted for in the constitutive modeling of skin tissues.

The literature related to modeling the behavior of soft biological tissues is vast. Accordingly, only a brief overview of what is most relevant to our work is presented in what follows. Initial modeling research on soft biological tissues was purely phenomenological and mainly focused on describing the behavior of arteries, generally modeled as incompressible thick-walled cylindrical tubes [29–31]. While

---

[*] Corresponding author.
E-mail address: shawn.a.chester@njit.edu (S.A. Chester).

https://doi.org/10.1016/j.mechrescom.2023.104098
Received 22 February 2023; Accepted 23 March 2023
Available online 30 March 2023

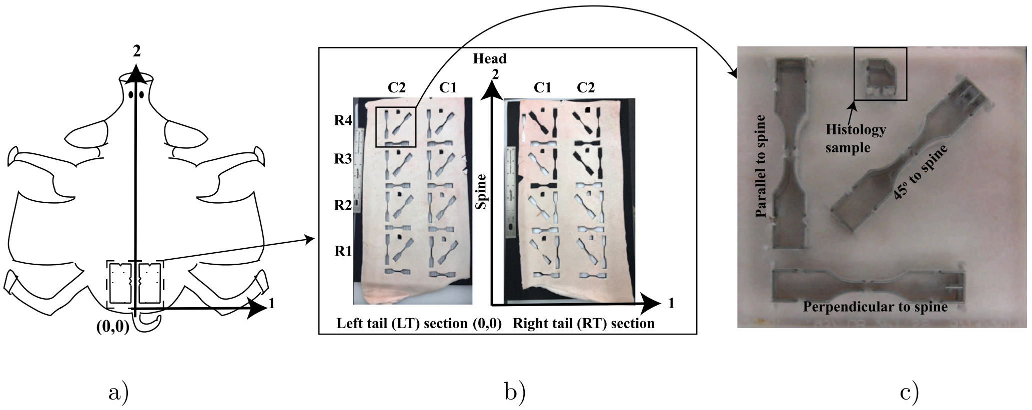

Fig. 1. (a) Schematic of the entire porcine skin showing the location from where the tissue sheets have been obtained for this work. (b) Representative image of the tissue sheets after tensile samples have been extracted. These sheets show various locations in row-column format (denoted by Ri and Cj) from where the test samples were extracted. (c) Image of our custom-made cutting die for the left side of the spine. For scale, the rulers in (b) are 6 in long. (For interpretation of the references to color in this figure legend, the reader is referred to the web version of this article.)

pure phenomenological models were a start, their lack of microstructural details, such as the embedded collagen fibers, left ample room for improvement, as our group found in prior work [25]. To explicitly account for fibers at a homogenized continuum scale, Holzapfel et al. [32] proposed a structure-based phenomenological model for arteries that considered the mean orientation of collagen fiber families. Later, that study was extended and improved to include the dispersion of collagen fiber families [33]. At present, the structure-based approach is generally considered the state-of-the-art for nearly all contemporary constitutive models for soft biological materials [12,34–39].

Although a lot has been done to characterize the mechanical response of various skin tissues, to the authors' knowledge, no prior work has yet considered tensile data from more than two orientations simultaneously to calibrate their respective constitutive model [12,19, 22]. We hypothesize that the collagen fiber families' properties such as cross-linking, density and undulation vary significantly between the spine and transverse to spine, and accordingly the mechanical behavior also varies. As such, to facilitate the development of more accurate models, our experimental data is collected from more than two orientations. Additionally, our previous work [28] shows that the in-plane fiber distribution is non-symmetric, but to our knowledge, no prior continuum-level model has taken that into account. Accordingly, experimental data from more than two orientations should be considered to develop a robust and enhanced model that can more accurately predict the mechanical behavior of skin tissues, along with the non-symmetric microstructural details of the in-plane fiber distribution.

In this work, we focus our experimental attention on porcine skin because it has similar mechanical characteristics to human skin [22,40–42] and is used in various medical devices [43]. The methodology developed for porcine skin can be applied to any soft tissue where collagen fibers are the main contributor. Also, porcine skin can be found in larger sizes and thus provide enough material to investigate the variability of mechanical response considering various locations.

Accordingly, the objectives of this paper are to (i) experimentally characterize the mechanical behavior of the porcine dermis in three distinct orientations, two orthogonal and one diagonal, and (ii) create and calibrate a robust structure-based constitutive model that can capture the experimental response from three orientations simultaneously. To accomplish this objective, first, through uniaxial tension testing, we measured the material response along the three orientations, parallel to the spine, perpendicular to the spine, and at an angle 45° to the spine. Then building upon the work of Holzapfel and co-workers [33,34,36], we have developed an enhanced structure-based model that takes into account: (i) the in-plane non-symmetry of the collagen fiber distribution and (ii) variation of the collagen fiber response along differently oriented tensile samples that we postulate to be due to changes in the local collagen fiber properties such as density, undulation and crosslinking etc., due to the fibers' engagement along the loading direction. The material parameters appearing in the model are calibrated by simultaneously considering the experimental tensile data obtained from these three different orientations.

The remainder of this paper is organized as follows. Section 2 describes the material used and the sample preparation procedure for tensile testing. Section 3 overviews the experimental tensile testing procedure and results of our experimental program. Section 4 discusses the details of our continuum-level modeling approach. Section 5 provides the results of model calibration, and Section 6 delivers some concluding remarks along with the future outlook.

2. Material and sample preparation

Porcine dermis produced by Midwest Research Swine (Glencoe, MN) has been used in this work, and we follow the same procedure for sample preparation as in our prior work [25]. Midwest Research Swine has an established quality-controlled process to provide high-quality porcine tissue and live research swine typically used for biomedical applications. At the Midwest Research Swine facility, the porcine skin was obtained from a six-month-old male 241-pound American Yorkshire–Landrace–Duroc, the skin was debristled, and the hypodermis was removed as per Midwest Research Swine's established process. Then tissue sheets were harvested in the form of rectangular sheets from the vicinity of the tail region of the porcine hide. The porcine tissue sheets were overnight delivered to the New Jersey Institute of Technology in a vacuum-sealed pouch, packaged with ice.

After receiving, the tissue sheets were stored in a freezer at −80 °C to prevent any degradation [44,45]. Preceding mechanical testing, the tissue sheets were defrosted for 24 h in a 4 °C refrigerator before preparing the samples for testing [46]. Fig. 1 gives an overview of how tensile samples are collected from the porcine tissue sheets. The sheets used in this work are taken from the left and right sides of the spine in the vicinity of the tail region, as shown in Fig. 1a. Two custom-made cutting dies based on the dimensions of ASTM D638-type V, one for each side of the spine, were used to produce the tensile samples along three orientations: parallel, perpendicular, and at 45° to the spine concurrently, keeping the orientations known with respect to the head and spine. Fig. 1b shows the various locations of the test samples in terms of rows and columns, and Fig. 1c shows an image of our custom-made cutting die for the left side of the spine. A die like this allows the simultaneous cutting of parallel, perpendicular, and 45° tensile samples. The right side cutting die is the mirror of the left cutting die. Further, according to our convention, the columns closer to the spine are labeled C1, and the columns away from the spine are labeled C2. And rows nearest to the tail are labeled as R1 that continue to increase, moving upward towards the head. We have also obtained the coordinates of the centers of all locations marked as rows and columns to have a physical sense of length scale. ImageJ software [47] has been used to obtain the coordinates of the locations corresponding to our rows and columns convention. The tensile samples were used to obtain the mechanical response of the material subjected to deformation. The test samples were cut utilizing a Tippmann Clicker 700 Die Cutting Press (Tippmann Industrial, Wayne, IN) with 7 tons of cutting pressure. The samples were then kept in an isotonic saline solution (Ricca Chemical 0.9% Sodium Chloride) until further testing.

3. Experiments

3.1. Experimental set-up and method

Uniaxial tension tests were performed on all samples to obtain the mechanical response as a function of various orientations following the same procedure as described in our prior work [25]. An MTS Criterion 43 uniaxial testing machine was used, and all experiments were conducted at room temperature. Before mechanical testing, the thicknesses of all the tensile samples were measured with an Electronic Drop Indicator (Mitutoyo 543-392, Mitutoyo Corporation, Kanagawa, Japan). The thickness of the gauge section was measured three times, and the average was taken for analysis. The tensile samples were speckled for Digital Image Correlation (DIC) analysis with 100-grit silicon carbide particles (Kingsley North, Norway, MI) applied to the skin surface with a hand-held pneumatic sprayer. DIC is a non-contact measuring technique that uses an optical method based on the images of deformation captured by a camera to track the deformation, which is more accurate than standard crosshead based measurements [48–50]. To perform a typical tensile test, a tensile sample was held between grips, and a constant engineering strain rate of $0.087\,\mathrm{s}^{-1}$ was prescribed to the crosshead to deform the sample till failure. This strain rate corresponds to a 50 mm/min crosshead velocity, corresponding to the documented rate for nonrigid ASTM tensile samples [51] and within the range of the previously reported rate porcine skin [22,23,27,52]. The resulting force signal is measured by a 1 kN load cell. Sample preconditioning was not performed to avoid irreversible damage to the skin tissue before testing [27], and all tensile samples were visibly wet during testing.

We used a data-acquisition software, VIC-2D (Correlated Solutions), coupled with a digital camera (Grasshopper3 USB3 made by Flir) to capture the images of the deformation and force data simultaneously during an experiment. That measured data allows us to compute the stretch and nominal (or engineering) stress using standard relations:

$$\lambda = \frac{l}{l_0}, \quad \text{and} \quad P = \frac{F}{A_0}\,. \tag{3.1}$$

Here, λ is the stretch in the loading direction, l is the instantaneous length of the gauge section during deformation, l_0 is the undeformed length of the gauge section, P is the nominal stress in the loading direction, F is the measured force, and A_0 is the cross-sectional area of gauge section of the undeformed sample. Further assuming incompressibility, the Cauchy stress was calculated using following relation

$$\sigma = \lambda\frac{F}{A_0}\,. \tag{3.2}$$

3.2. Uniaxial tensile results

Figs. 2 and 3 show the results of the uniaxial tension tests of all samples. We note that location LT R2C2 shows the experimental data only for the parallel sample and 45°, no data for the sample perpendicular to the spine, as it slipped during the experiment. Similarly, no experimental data could be obtained for RT R1C1. The tension test results demonstrate that the porcine skin exhibits non-linear anisotropic behavior. All the curves clearly follow the same trend with classic toe, non-lienar, and linear regions; still, the specific response varies due to the variation of the collagen fiber density and other microstructural details with specific locations and orientations. It can be seen that for the locations closer to the spine (labeled as C1), for both the left and the right sides of the spine, the samples oriented at 45° to the spine have the stiffest response, whereas the samples parallel to the spine shows the least stiff response. In contrast, for the samples taken from locations further away from the spine (labeled as C2), the samples oriented at 45° to the spine have the least stiff response, whereas the samples perpendicular to the spine have the stiffest response. This shows that the material response shows symmetry with respect to the spine, and the specific material response changes with orientation for various locations. Overall this implies that variations in the underlying collagen microstructure, such as the fiber density and undulation for various locations, drive the mechanical response.

4. Constitutive model

The continuum framework used to describe the mechanical behavior of the porcine dermis is summarized in this section. We build upon the structure-based model originally reported by Gasser et al. [33] for arteries, with enhancements aimed at more robustly describing the behavior of skin.

4.1. Kinematics

Consider a reference body $\mathcal{B}_\mathrm{R}$ identified with the region of space it occupies in a fixed reference configuration, and denote by $\mathbf{x}_\mathrm{R}$, an arbitrary material point of $\mathcal{B}_\mathrm{R}$. The referential body $\mathcal{B}_\mathrm{R}$ then undergoes a motion $\mathbf{x} = \chi(\mathbf{x}_\mathrm{R}, t)$ to the deformed body $\mathcal{B}_t$ with deformation gradient given by[1]

$$\mathbf{F} = \nabla\chi, \quad \text{such that} \quad J = \det\mathbf{F} > 0. \tag{4.1}$$

Here J is a measure of the volume change produced by the deformation, also called the Jacobian of the deformation. The left and right Cauchy–Green tensors are defined as

$$\mathbf{B} = \mathbf{F}\mathbf{F}^\top, \quad \mathbf{C} = \mathbf{F}^\top\mathbf{F}, \tag{4.2}$$

respectively. To accommodate embedded collagen fibers in skin tissues, we assume that two distinct sets of fiber families, each indicated by "i", are present in the body $\mathcal{B}_\mathrm{R}$. Each fiber family is characterized by a mean direction denoted by the referential unit vector $\mathbf{a}_\mathrm{R}^{(i)}$ and the associated structure tensor $\mathbf{A}_\mathrm{R}^{(i)}$ for each fiber family is given by

$$\mathbf{A}_\mathrm{R}^{(i)} \overset{\text{def}}{=} \mathbf{a}_\mathrm{R}^{(i)} \otimes \mathbf{a}_\mathrm{R}^{(i)}\,. \tag{4.3}$$

As is standard in the literature, we employ a multiplicative decomposition of the deformation gradient into volumetric and distortional components. The decomposition is given by

$$\mathbf{F} = \mathbf{F}_\mathrm{vol}\mathbf{F}_\mathrm{dis}\,, \tag{4.4}$$

where

$$\mathbf{F}_\mathrm{vol} \overset{\text{def}}{=} J^{1/3}\mathbf{1}\,, \quad \text{and} \quad \mathbf{F}_\mathrm{dis} \overset{\text{def}}{=} J^{-1/3}\mathbf{F} \quad \text{such that} \quad \det\mathbf{F}_\mathrm{dis} = 1\,, \tag{4.5}$$

with $\mathbf{1}$ the identity tensor. The corresponding distortional left and right Cauchy–Green tensors are

$$\mathbf{B}_\mathrm{dis} = \mathbf{F}_\mathrm{dis}\mathbf{F}_\mathrm{dis}^\top = J^{-2/3}\mathbf{B}\,, \quad \text{and} \quad \mathbf{C}_\mathrm{dis} = \mathbf{F}_\mathrm{dis}^\top\mathbf{F}_\mathrm{dis} = J^{-2/3}\mathbf{C}\,. \tag{4.6}$$

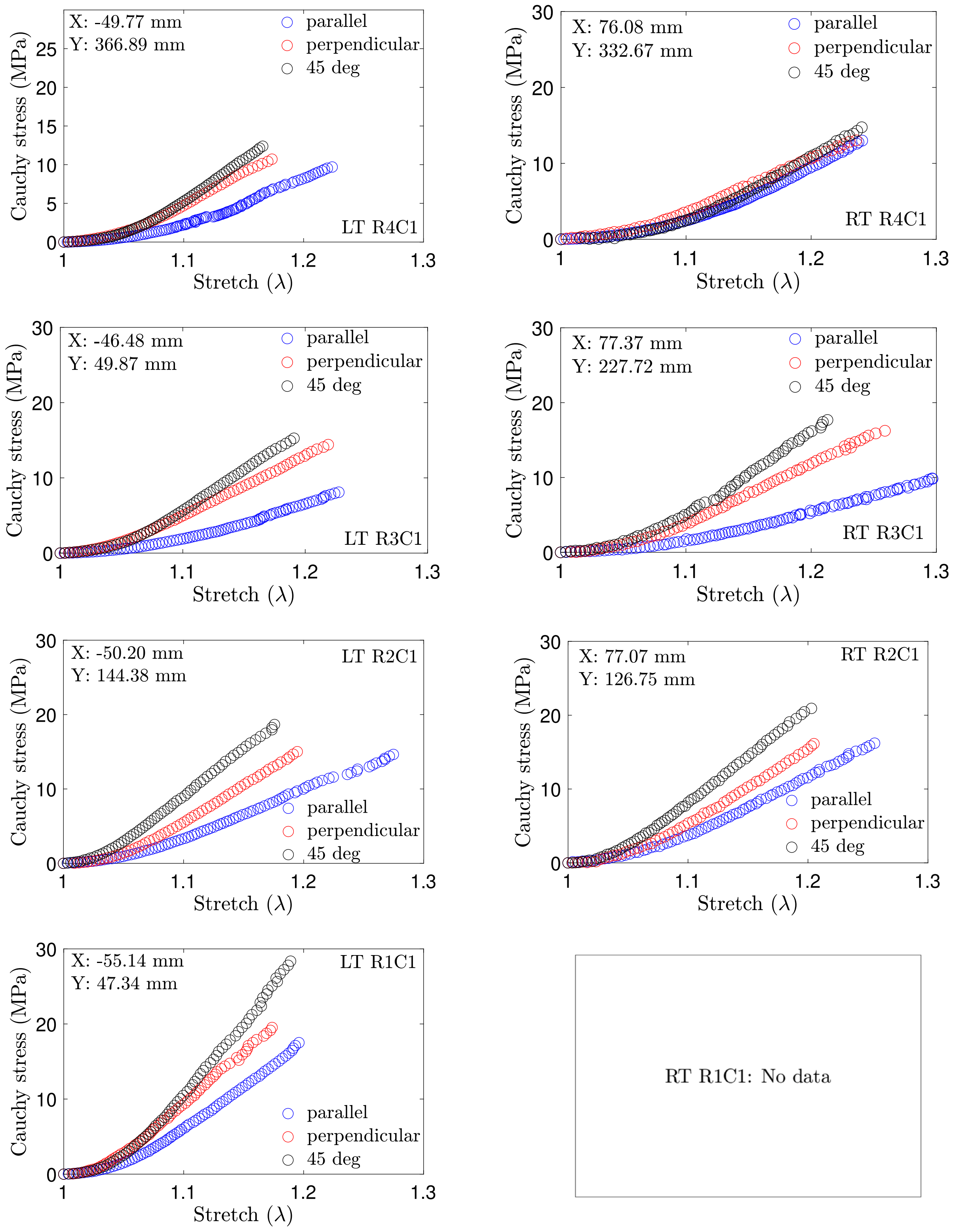

Fig. 2. Uniaxial tension test results of the various samples taken from column C1, cf., Fig. 1.

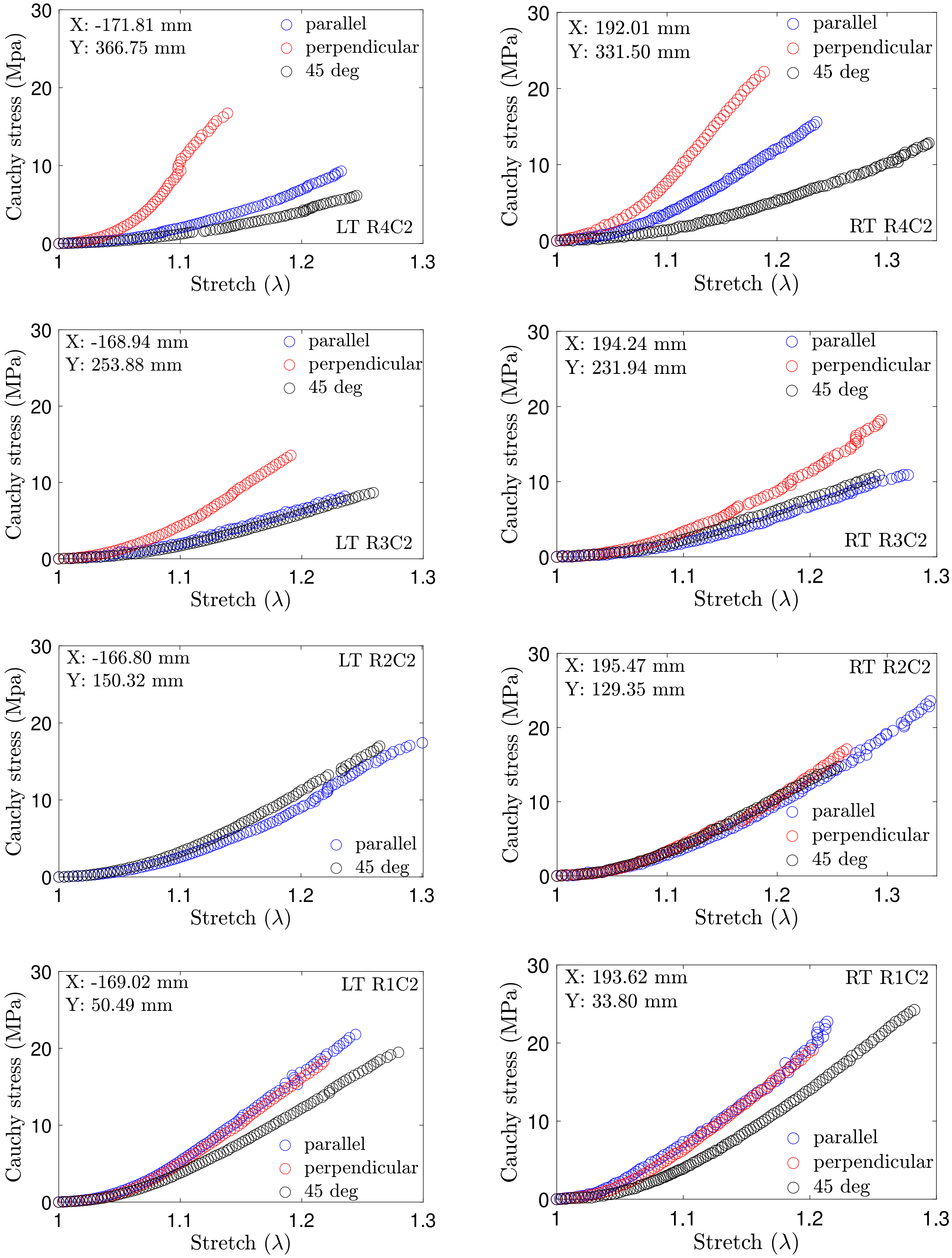

Fig. 3. Uniaxial tension test results of the various samples taken from column C2, cf., Fig. 1.

Table 1
List of structural parameters for the symmetric distribution, reproduced from our previous work on the same material [28].

Location R_xC_y	Coordinates taking tail as origin (mm)	Symmetric		
		$\mathbf{a}_R^{(1)}$	$\mathbf{a}_R^{(2)}$	κ_{ip}
LT R4C1	X: −49.77 Y: 366.89	[0.867; −0.498;0]	[0.867; 0.498;0]	0.165
LT R4C2	X: −171.81 Y: 366.75	[0.894; −0.449;0]	[0.894; 0.449;0]	0.206
LT R3C1	X: −46.48 Y: 249.87	[0.796; −0.605;0]	[0.796; 0.605;0]	0.181
LT R3C2	X: −168.94 Y: 253.88	[0.873; −0.488;0]	[0.873; 0.488;0]	0.260
LT R2C1	X: −50.20 Y: 144.38	[0.779; −0.627;0]	[0.779; 0.627;0]	0.139
LT R1C1	X: −55.14 Y: 47.34	[0.822; −0.569;0]	[0.822; 0.569;0]	0.123
LT R1C2	X: −169.02 Y: 50.49	[0.921; −0.390;0]	[0.921; 0.390;0]	0.254
RT R4C1	X: 76.08 Y: 332.67	[0.797; −0.604;0]	[0.797; 0.604;0]	0.133
RT R4C2	X: 192.01 Y: 331.50	[0.860; −0.511;0]	[0.860; 0.511;0]	0.160
RT R3C1	X: 77.37 Y: 227.73	[0.727; −0.687;0]	[0.727; 0.687;0]	0.099
RT R3C2	X: 194.24 Y: 231.94	[0.808; −0.590;0]	[0.808; 0.590;0]	0.181
RT R2C1	X: 77.07 Y: 126.75	[0.688; −0.725;0]	[0.688; 0.725;0]	0.104
RT R2C2	X: 195.47 Y: 129.35	[0.692; −0.722;0]	[0.692; 0.722;0]	0.123
RT R1C2	X: 193.62 Y: 33.80	[0.708; −0.706;0]	[0.708; 0.706;0]	0.149

LT: Left Tail; RT: Right Tail

4.2. *Free energy*

We build our model based on the seminal work of Gasser et al. [33] which includes both the orientation and dispersion of the embedded fibers and is considered the current state-of-the-art for constitutive modeling to characterize the mechanical behavior of any soft biological tissue. Gasser et al. [33] was based on the three-dimensional spatial distribution of collagen fibers considering rotational symmetry. For a planar fiber distribution the two dimensional version of Gasser et al. [33] was discussed in Ogden [53] and Cortes et al. [54], which was later used in Holzapfel and Ogden [34] and Holzapfel et al. [36].

4.2.1. *Free energy of the baseline model*

The overall free energy density per unit reference volume for two symmetric fiber families with dispersion based on Gasser et al. [33] is given in the form:

$$\psi_{\mathrm{R}}(J, \mathbf{C}_{\mathrm{dis}}, \mathbf{H}^{(i)}_{\mathrm{sym}}) = \underbrace{\frac{K}{2}(\ln J)^2}_{\text{volumetric contribution}} + \underbrace{\frac{1}{2}\mu(\mathrm{tr}\,\mathbf{C}_{\mathrm{dis}} - 3)}_{\text{ground substance}} + \underbrace{\sum_{i=1}^{2} \frac{k_1}{2k_2}\left\{\exp\left[k_2(\mathbf{H}^{(i)}_{\mathrm{sym}} : \mathbf{C}_{\mathrm{dis}} - 1)^2\right] - 1\right\}}_{\text{embedded fibers}} . \tag{4.7}$$

The distortional (non-volumetric) contribution of the free energy is decomposed into two parts, one to account for the soft and isotropic ground substance, and the second to account for the collagen fibers that impart the anisotropy. Here $\mathbf{H}^{(i)}_{\mathrm{sym}}$ is the generalized structural tensor for each fiber family that includes both the dispersion and mean orientation based on symmetric fiber distribution. From the recent literature [cf., e.g., [36], and references therein] we have the following relation for $\mathbf{H}^{(i)}_{\mathrm{sym}}$, for the in-plane collagen fiber dispersion

$$\mathbf{H}^{(i)}_{\mathrm{sym}} = \kappa_{ip}\mathbf{1}_2 + \left(1 - 2\kappa_{ip}\right)\mathbf{a}^{(i)}_{\mathrm{R}} \otimes \mathbf{a}^{(i)}_{\mathrm{R}} . \tag{4.8}$$

Here, i indicates the fiber family, $i = 1, 2$; $\mathbf{1}_2$ is the two-dimensional identity tensor; μ, k_1, k_2, and K are the *material parameters*. μ is the shear modulus of the ground substance. $k_1 > 0$ is stress dimensioned parameter and $k_2 > 0$ is a dimensionless parameter that together define the collagen fiber response. To approximate the near incompressibility of the dermis, the bulk modulus, K, is taken as three orders of magnitudes larger than the shear modulus μ. $0 \leq \kappa_{ip} \leq 1/2$ is the planar dispersion, and $\mathbf{a}^{(i)}_{\mathrm{R}}$ is the referential unit vector along the mean collagen fiber direction per family in the reference configuration. Together, the dispersion and mean direction are called *structural parameters*.

We note that each fiber family shares the same value of the material parameters k_1 and k_2, as well as magnitude of dispersion, and that the mean orientations are symmetrically aligned for a symmetric fiber distribution.

Lastly, the Cauchy stress, corresponding to the free energy density function (4.7), is given by

$$\begin{aligned}\mathbf{T} = J^{-1}\left[K(\ln J)\mathbf{1} + \mu\left\{\mathbf{B}_{\mathrm{dis}} - \frac{1}{3}(\mathrm{tr}\,\mathbf{B}_{\mathrm{dis}})\mathbf{1}\right\}\right] + \\ 2k_1 J^{-5/3}\sum_{i=1}^{2}\Bigg\{\left[\exp[k_2(\mathbf{H}^{(i)}_{\mathrm{sym}} : \mathbf{C}_{\mathrm{dis}} - 1)^2]\right]\left[(\mathbf{H}^{(i)}_{\mathrm{sym}} : \mathbf{C}_{\mathrm{dis}} - 1)\right] \\ \times\left[\mathbf{F}\mathbf{H}^{(i)}_{\mathrm{sym}}\mathbf{F}^{\top} - \frac{1}{3}(\mathbf{H}^{(i)}_{\mathrm{sym}} : \mathbf{C}_{\mathrm{dis}})J^{2/3}\mathbf{1}\right]\Bigg\} .\end{aligned} \tag{4.9}$$

In the remainder of this paper, the term *baseline model* is defined by the specific choice of free energy (4.7) together with the generalized structural tensor (4.8), leading to Cauchy stress (4.9).

4.2.2. *Free energy of the enhanced model*

While the prior literature has been successful at modeling the response of many different tissues, our enhanced model incorporates a few improvements to more accurately capture the tensile response from three orientations simultaneously and account for non-symmetric fiber distribution. There are three main departures that make this work distinct: (1) the generalized structure tensor is taken to be non-symmetric for the in-plane fiber distribution; (2) each of the fiber families is characterized by its own distinct set of material parameters, to capture the varying fiber response of differently oriented tensile samples; and (3) the ground substance response to loading is modeled as "exponential". The following paragraphs list arguments for each change in more detail.

First, histology results from our recent work Jaiswal et al. [28] indicates that an improvement in capturing fiber orientations as significant as 200% may be achieved by using a non-symmetric fiber distribution over a symmetric one. Accordingly, we modify (4.8) such that the observed non-symmetric is taken into account through a generalized structure tensor $\mathbf{H}^{(i)}_{\text{non-sym}}$ for each fiber family.

Second, the results of our experiments, as shown in Figs. 2 and 3, clearly indicate that the behavior changes with orientation and location. Since histology information is already known for each location, the structural parameters associated with fiber family's directionality and dispersion can be assumed known. A proper application of (4.7) would indicate that a single value for μ, k_1, and k_2 for the two fiber families is all that is needed to model the behavior at each location. However, we found that this is not the case here, and taking some inspiration from Han [39] we allow for each fiber family to take on its

---

[1] The symbol ∇ denotes the gradient with respect to the material point $\mathbf{x}_{\mathrm{R}}$ in the reference configuration.

Table 2

List of structural parameters for the non-symmetric fiber distribution, reproduced from our previous work on the same material [28].

Location R_xC_y	Coordinates taking tail as origin (mm)	Non-symmetric			
		$\mathbf{a}_{\mathrm{R}}^{(1)}$	$\mathbf{a}_{\mathrm{R}}^{(2)}$	$\kappa_{ip}^{(1)}$	$\kappa_{ip}^{(2)}$
LT R4C1	X: −49.77 Y: 366.89	[0.811; −0.585; 0.000]	[0.914; 0.405; 0.000]	0.147	0.159
LT R4C2	X: −171.81 Y: 366.75	[0.902; −0.432; 0.000]	[0.885; 0.466; 0.000]	0.203	0.208
LT R3C1	X: −46.48 Y: 249.87	[0.912; −0.411; 0.000]	[0.730; 0.683; 0.000]	0.264	0.102
LT R3C2	X: −168.94 Y: 253.88	[0.840; −0.542; 0.000]	[0.934; 0.358; 0.000]	0.217	0.317
LT R2C1	X: −50.20 Y: 144.38	[0.830; −0.558; 0.000]	[0.747; 0.665; 0.000]	0.207	0.092
LT R1C1	X: −55.14 Y: 47.34	[0.862; −0.507; 0.000]	[0.801; 0.599; 0.000]	0.199	0.078
LT R1C2	X: −169.02 Y: 50.49	[0.952; −0.305; 0.000]	[0.891; 0.455; 0.000]	0.271	0.232
RT R4C1	X: 76.08 Y: 332.67	[0.760; −0.649; 0.000]	[0.823; 0.568; 0.000]	0.181	0.091
RT R4C2	X: 192.01 Y: 331.50	[0.895; −0.447; 0.000]	[0.794; 0.608; 0.000]	0.095	0.210
RT R3C1	X: 77.37 Y: 227.73	[0.684; −0.729; 0.000]	[0.789; 0.615; 0.000]	0.058	0.157
RT R3C2	X: 194.24 Y: 231.94	[0.777; −0.629; 0.000]	[0.830; 0.558; 0.000]	0.278	0.116
RT R2C1	X: 77.07 Y: 126.75	[0.716; −0.698; 0.000]	[0.659; 0.752; 0.000]	0.102	0.100
RT R2C2	X: 195.47 Y: 129.35	[0.595; −0.804; 0.000]	[0.779; 0.627; 0.000]	0.085	0.110
RT R1C2	X: 193.62 Y: 33.80	[0.572; −0.820; 0.000]	[0.822; 0.569; 0.000]	0.085	0.119

LT: Left Tail; RT: Right Tail

own set of material properties, namely $k_1^{(i)}$ and $k_2^{(i)}$. In addition to that, we allow the stiffness to be associated with underlying microstructure through the use of $\mathbf{H}_{\text{non-sym}}^{(i)}$ and deformation to more accurately capture the tensile response in three distinct orientations, simultaneously. This assumption regarding fiber material parameters is our attempt to capture changes in the micro-structural details, such as the collagen fiber density and undulation, due to engagement of fibers along the loading direction, that are currently not explicitly addressed in the prior literature.

Third, based on the recent work of Bai et al. [55], using a Neo-Hookean model for the ground substance results in unphysical model behaviors under certain loading conditions. Accordingly, we follow Bai et al. [55] and further modify (4.7) such that the ground substance is modeled with an exponential form of strain energy density function.

After incorporating all these modifications to (4.7), and keeping the notation i to indicate the fiber family, our enhanced free energy function is given by

$$\psi_{\mathrm{R}}(J, \mathbf{C}_{\mathrm{dis}}, \mathbf{H}_{\text{non-sym}}^{(i)}) = \underbrace{\frac{K}{2}(\ln J)^2}_{\text{volumetric contribution}} + \underbrace{\frac{\mu}{2\beta}\left\{\exp[\beta\left(\operatorname{tr}\mathbf{C}_{\mathrm{dis}} - 3\right)] - 1\right\}}_{\text{ground substance}} + \underbrace{\sum_{i=1}^{2} \frac{k_1^{(i)}\left(\mathbf{H}_{\text{non-sym}}^{(i)} : \mathbf{C}_{\mathrm{dis}}\right)}{2k_2^{(i)}} \{\exp\left[\, k_2^{(i)}(\mathbf{H}_{\text{non-sym}}^{(i)} : \mathbf{C}_{\mathrm{dis}} - 1)^2 \,\right] - 1\}}_{\text{embedded fibers}} . \tag{4.10}$$

Here, unlike (4.7) each fiber family uses distinct values of the material parameters $k_1^{(i)}$ and $k_2^{(i)}$. And β is a dimensionless material parameter for the ground substance [55].

Further, $\mathbf{H}_{\text{non-sym}}^{(i)}$ is taken in the form

$$\mathbf{H}_{\text{non-sym}}^{(i)} = \kappa_{ip}^{(i)}\mathbf{1}_2 + (1 - 2\kappa_{ip}^{(i)})\mathbf{a}_{\mathrm{R}}^{(i)} \otimes \mathbf{a}_{\mathrm{R}}^{(i)}\,; \quad 0 \le \kappa_{ip}^{(i)} \le 1/2\,. \tag{4.11}$$

Here, $\kappa_{ip}^{(i)}$ and $\mathbf{a}_{\mathrm{R}}^{(i)}$ characterize the fiber distribution in the plane of the dermis, specifically $\kappa_{ip}^{(i)}$ is the planar fiber dispersion for each fiber family, and $\mathbf{a}_{\mathrm{R}}^{(i)}$ is the referential unit vector in the direction of the mean orientation associated with each fiber family. And unlike the symmetric form in (4.8), here each collagen fiber family has its own independent dispersion and mean orientation obtained through histological analysis.

The Cauchy stress corresponding to our enhanced free energy function is given by

$$\begin{aligned}
\mathbf{T} = J^{-1} \Big[& K(\ln J)\mathbf{1} + \mu\left\{\exp[\beta\left(\operatorname{tr}\mathbf{C}_{\mathrm{dis}} - 3\right)]\right\}\left\{\mathbf{B}_{\mathrm{dis}} - \frac{1}{3}(\operatorname{tr}\mathbf{B}_{\mathrm{dis}})\mathbf{1}\right\}\Big] + \\
& \sum_{i=1}^{2}\Bigg\{ 2k_1^{(i)}\left(\mathbf{H}_{\text{non-sym}}^{(i)} : \mathbf{C}_{\mathrm{dis}}\right)J^{-5/3}\left[\exp[k_2^{(i)}(\mathbf{H}_{\text{non-sym}}^{(i)} : \mathbf{C}_{\mathrm{dis}} - 1)^2]\right] \\
& \times \left[(\mathbf{H}_{\text{non-sym}}^{(i)} : \mathbf{C}_{\mathrm{dis}} - 1)\right] \\
& \times \left[\mathbf{F}\mathbf{H}_{\text{non-sym}}^{(i)}\mathbf{F}^{\top} - \frac{1}{3}(\mathbf{H}_{\text{non-sym}}^{(i)} : \mathbf{C}_{\mathrm{dis}})J^{2/3}\mathbf{1}\right]\Bigg\} + \\
& \sum_{i=1}^{2}\Bigg\{ J^{-5/3}\left(\frac{k_1^{(i)}}{k_2^{(i)}}\right)\left[\mathbf{F}\mathbf{H}_{\text{non-sym}}^{(i)}\mathbf{F}^{\top} - \frac{1}{3}(\mathbf{H}_{\text{non-sym}}^{(i)} : \mathbf{C}_{\mathrm{dis}})J^{2/3}\mathbf{1}\right] \\
& \times\left[\exp[k_2^{(i)}(\mathbf{H}_{\text{non-sym}}^{(i)} : \mathbf{C}_{\mathrm{dis}} - 1)^2] - 1\right]\Bigg\}.
\end{aligned} \tag{4.12}$$

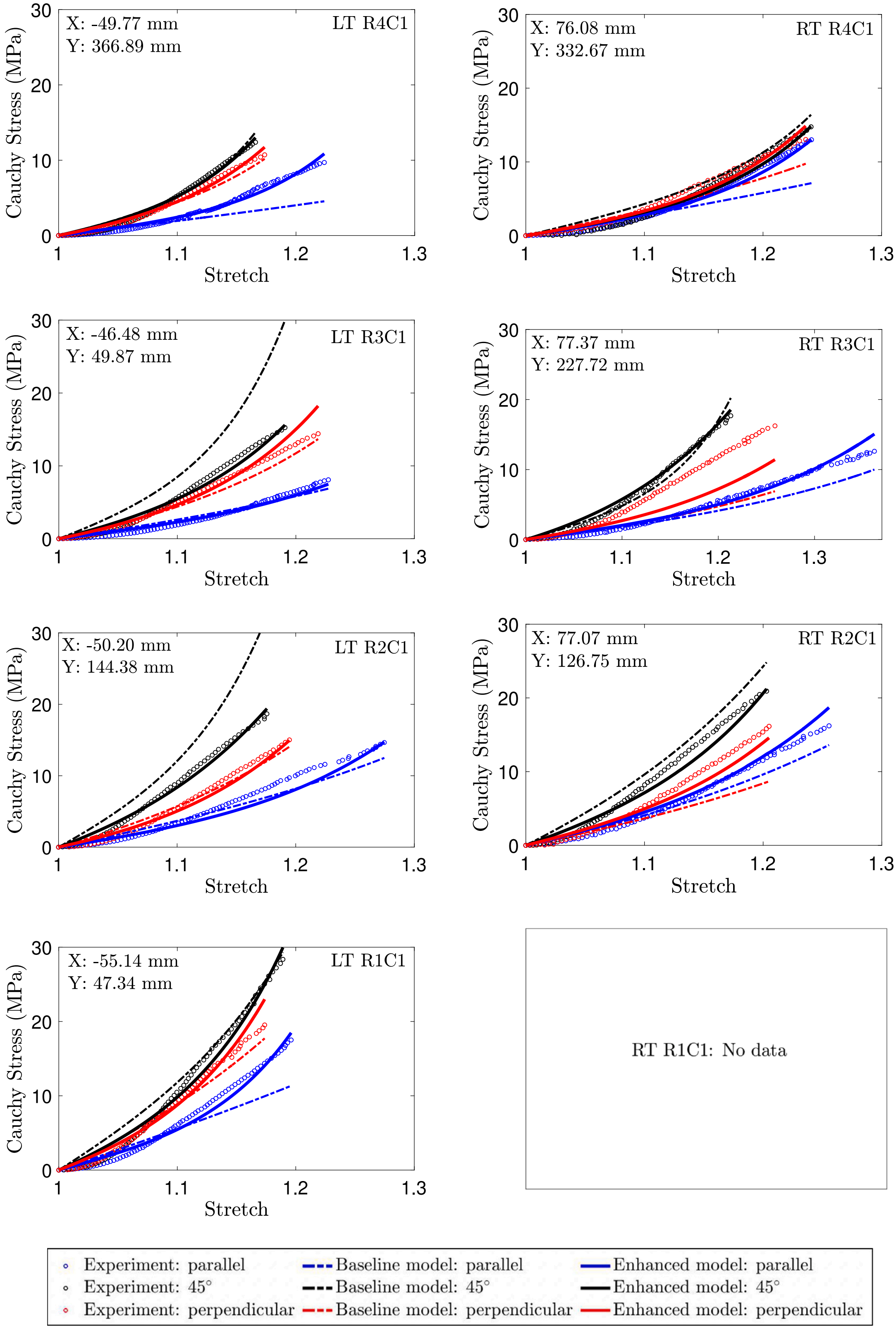

Fig. 4. Calibration results of our enhanced model and the baseline model using the uniaxial tension test data for the samples taken from column C1.

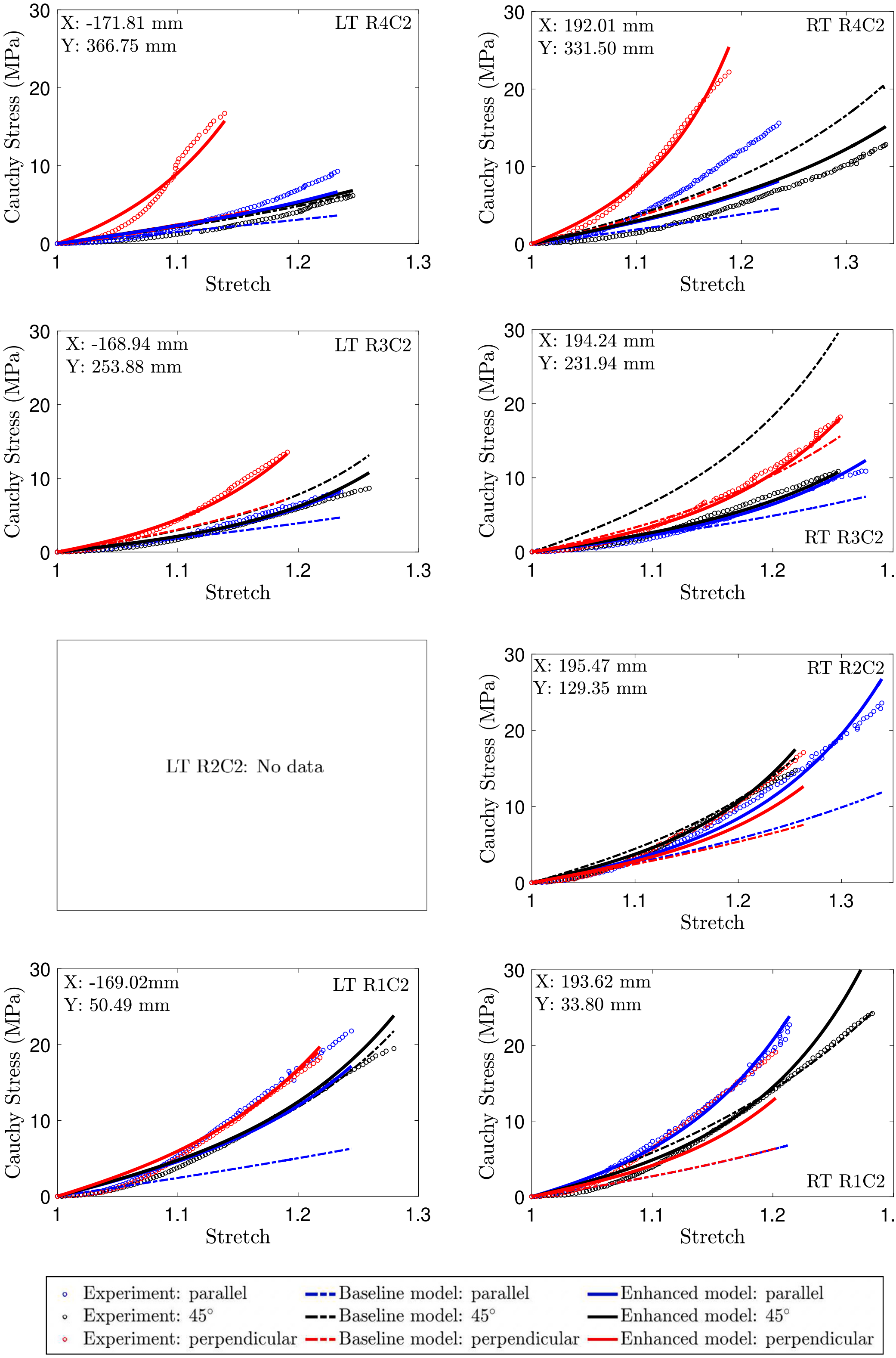

Fig. 5. Calibration results of our enhanced model and the baseline model using the uniaxial tension test data for the samples taken from column C2.

Table 3
List of material parameters obtained by calibration of the baseline model with the experimental data of tensile samples taken in three orientations from different locations.

Location R_xC_y	Coordinates taking tail as origin (mm)	μ (MPa)	k_1 (MPa)	k_2
LT R4C1	X: −49.77 Y: 366.89	6.410	9.940	13.530
LT R4C2	X: −171.81 Y: 366.75	4.999	3.006	2.057
LT R3C1	X: −46.48 Y: 249.87	7.896	17.900	9.458
LT R3C2	X: −168.94 Y: 253.88	5.998	6.501	7.093
LT R2C1	X: −50.20 Y: 144.38	11.002	22.002	6.2199
LT R1C1	X: −55.14 Y: 47.34	18.035	17.250	3.318
LT R1C2	X: −169.02 Y: 50.49	8.011	15.965	4.471
RT R4C1	X: 76.08 Y: 332.67	9.002	4.198	4.231
RT R4C2	X: 192.01 Y: 331.50	6.070	6.918	1.008
RT R3C1	X: 77.37 Y: 227.73	5.001	7.001	5.005
RT R3C2	X: 194.24 Y: 231.94	6.772	15.992	2.748
RT R2C1	X: 77.07 Y: 126.75	9.864	16.280	1.003
RT R2C2	X: 195.47 Y: 129.35	6.990	6.070	1.420
RT R1C2	X: 193.62 Y: 33.80	6.990	10.899	0.727

LT: Left Tail; RT: Right Tail

In the remainder of this paper, the term *enhanced model* is defined by the specific choice of free energy (4.10) together with the generalized structural tensor (4.11), leading to Cauchy stress (4.12).

5. Enhanced model results

5.1. Model calibration and comparison

Both the baseline model and our new enhanced model are calibrated to our experimental data so that we may make comparisons. For the structural parameters, values are taken directly from our prior histology work [28]. Table 1 summarizes the structural parameters for the symmetric fiber distribution used with (4.8), and Table 2 provides structural parameters for our enhanced model used by (4.11). For the material parameters, the calibration is performed using the MATLAB built-in least squares function `lsqnonlin`. Due to the anisotropic nature of this material, the choice of parameters affects the transverse deformations. Therefore, all non-prescribed components of the deformation gradient are found through an iterative process, ensuring stress-free conditions on the traction-free surfaces. The calibrated material parameters for the baseline model using (4.9) and our enhanced model using (4.12) are provided in Tables 3 and 4 for all locations, respectively.

Figs. 4 and 5 show the calibrated model results for all samples. The enhanced model conforms well with experimental data of all tensile samples from three orientations, parallel to the spine, perpendicular to the spine, and 45° to the spine for all the locations, as opposed to the baseline model. Additionally, to quantify the quality of both models, we have calculated the root mean square error (RMSE) for all the experimental samples considered in the analysis. We performed a Wilcoxon rank sum test analysis on the RMSE values of both the baseline model and enhanced model to demonstrate the difference between the two models is statistically significant. We found that the distribution is not-normal, and the p-value obtained from the analysis was 8.84×10^{-7}, which indicates the difference between both the models is statistically significant since our p-value is less than 0.05. Fig. 6 shows the box plots of RMSE for both models, demonstrating the improvement by our enhanced model. The main takeaway from Fig. 6 is that the enhanced model works very well for more than 75% of the experiments with six outliers, whereas the baseline model is only working well for 25% of the experimental data. For completeness, Table 5 summarizes the root mean square error (RMSE) values of both models. We can see that we have forty-two tensile samples from fourteen locations, and the enhanced model shows improvement over 88% cases compared to the baseline model. In 13 out of 42, instances, the improvement is three orders of magnitude over the baseline model.

5.2. Model capabilities

The constitutive models are numerically implemented in Abaqus/Explicit [56] to demonstrate the model capabilities in a complex three-dimensional loading scenario by writing a user-defined material subroutine (VUMAT). We consider a thin rectangular strip to simulate the behavior of a sample of porcine dermis under combined displacement and pressure loading.

The geometry we consider is a rectangular specimen with a width of 300 mm, height = 150 mm, and thickness = 2.25 mm, and boundary conditions are shown in Fig. 7a. The orientations of the embedded fibers are measured with respect to direction 1. The structural and material parameters required for the respective models are taken from location LTR3C1. For the baseline model, these parameters are taken from Tables 1 and 3, respectively. And for the enhanced model, the respective parameters are taken from Tables 2 and 4. The entire body is meshed with 720 C3D8R elements. The simulation consists of three steps to create a complex loading — in the first step, a deformation is prescribed; in the second step, pressure loading is applied; and in the last step, all previously prescribed conditions are held fixed. Referring to Fig. 7a, for boundary conditions, the left face *ABEH* is held fixed for all steps, and in the first step, a displacement u = 25 mm is prescribed on the right face *CDGF* only in direction 1 while keeping the displacement in directions 2 and 3 fixed. That prescribed displacement is held fixed during the subsequent steps. Further, the movement for the top face *BCFE* and bottom face *ADGH* is also fixed in directions 2 and 3 in all steps. In the second loading step, a uniformly distributed pressure P of 172 kPa is applied on face *HGFE*. And in the last step, the sample is held with all the previously applied boundary conditions. Fig. 7b shows the prescribed displacement and pressure loading profile. Fig. 8a and b show the results of this simulation for the baseline model as well as our enhanced model, respectively. They compare contours of u_3 for the rectangular strip after applying the pressure. It can be seen that the simulated displacement fields between these two cases are different. Fig. 8c shows a comparison of the peak displacement u_3 for the two models, giving a difference of roughly 12.8%. This indicates that the models respond differently under the same loading condition, and the difference is noticeable. Based on our analysis summarized in Fig. 6, the enhanced model is more accurate than the baseline model. This suggests that the enhanced model will better predict the mechanical response of soft biological tissues and may serve as an aid to designers of medical devices.

Table 4
List of material parameters obtained by calibration of our enhanced model with the experimental data of tensile samples taken in three orientations from different locations.

Location $R_x C_y$	Coordinates taking tail as origin (mm)	μ (MPa)	β	$k_1^{(1)}$ (MPa)	$k_1^{(2)}$ (MPa)	$k_2^{(1)}$	$k_2^{(2)}$
LT R4C1	X: −49.77 Y: 366.89	6.537	6.514	6.937	6.857	4.351	2.062
LT R4C2	X: −171.81 Y: 366.75	7.433	1.319	0.154	74.564	1.020	9.992
LT R3C1	X: −46.48 Y: 249.87	6.667	2.735	20.073	3.575	4.842	3.364
LT R3C2	X: −168.94 Y: 253.88	6.056	3.917	0.079	24.041	0.437	2.212
LT R2C1	X: −50.20 Y: 144.38	7.906	1.625	16.526	45.546	1.309	3.031
LT R1C1	X: −55.14 Y: 47.34	14.452	7.001	13.692	15.943	2.922	1.477
LT R1C2	X: −169.02 Y: 50.49	13.927	3.161	1.385	7.468	1.741	3.179
RT R4C1	X: 76.08 Y: 332.67	7.717	4.820	8.761	0.954	2.350	2.575
RT R4C2	X: 192.01 Y: 331.50	8.903	1.633	20.492	0.100	9.933	1.051
RT R3C1	X: 77.37 Y: 227.73	5.896	1.819	1.043	10.781	0.490	0.243
RT R3C2	X: 194.24 Y: 231.94	5.906	1.930	39.317	1.784	5.365	1.184
RT R2C1	X: 77.07 Y: 126.75	11.196	1.478	49.587	6.086	19.781	1.768
RT R2C2	X: 195.47 Y: 129.35	7.833	3.144	4.162	2.264	1.672	1.501
RT R1C2	X: 193.62 Y: 33.80	11.178	5.101	20.388	1.497	1.349	1.120

LT: Left Tail; RT: Right Tail

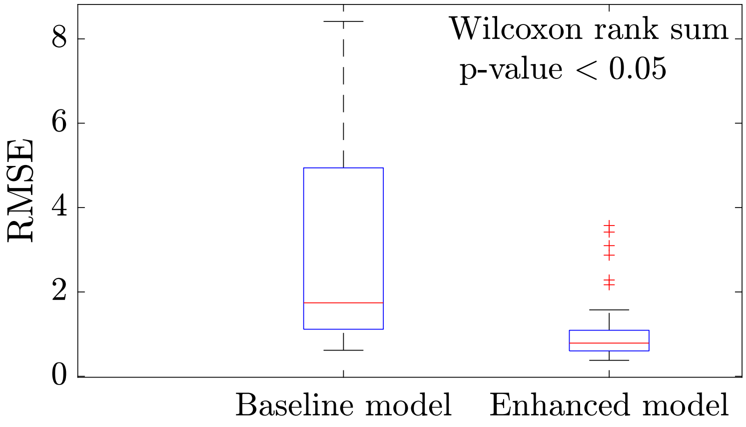

Fig. 6. Box plot comparing RMSE values obtained from the calibration of experimental data for all forty-two samples from different locations using the baseline model and our enhanced model.

6. Concluding remarks

We have experimentally demonstrated that porcine dermis exhibits non-linear, anisotropic behavior with symmetry with respect to the spine. We employed the structural parameters from our previous work [28] and used the prior literature [33,39,53–55] as a base to develop an enhanced structure-based model. We have demonstrated that the current state-of-the-art models may be improved with a few enhancements. Our enhancements include: (i) modified structure tensor to capture the non-symmetric in-plane fiber distribution; (ii) using the distinct sets material parameters $k_1^{(i)}$ and $k_2^{(i)}$ along with structural and deformation dependent collagen material parameters to account for the variations in collagen fiber properties with location and tensile sample orientation; and lastly, (iii) using an exponential-based function for the ground substance response that takes care of the non-linearity of the ground substance postulated in Bai et al. [55]. Our enhanced model was calibrated using the data from a series of uniaxial experiments by employing a non-linear least squares method. The performance of the

Table 5
Summary of RMSE values for the baseline model and our enhanced model.

Location R_xC_y	Coordinates taking tail as origin (mm)	Sample Orientation (θ)	Baseline model, RMSE	Enhanced model, RMSE	% improvement by enhanced model
		Parallel	2.0681	0.3787	138.09%
LT R4C1	X: −49.77	45°	0.6170	0.5369	13.88%
	Y:366.89	Perpendicular	0.6549	0.4095	46.11%
		Parallel	2.4185	1.0311	80.44%
LT R4C2	X: −171.81	45°	0.6821	0.8384	−20.56%
	Y: 366.75	Perpendicular	7.5128	1.3691	138.34%
		Parallel	1.0194	0.5542	54.28%
LT R3C1	X: −46.48	45°	5.1731	0.7195	151.16%
	Y: 249.87	Perpendicular	0.9129	0.9681	−5.87%
		Parallel	1.594	0.3823	122.62%
LT R3C2	X: −168.94	45°	1.7906	0.6026	99.28%
	Y: 253.88	Perpendicular	2.9606	0.5199	140.25%
		Parallel	1.1708	1.0704	8.96%
LT R2C1	X: −50.20	45°	5.0680	0.6479	154.66%
	Y: 144.38	Perpendicular	0.8058	0.7205	11.18%
		Parallel	2.5129	0.7537	107.71%
LT R1C1	X: −55.14	45°	1.6498	1.0913	40.75%
	Y: 47.34	Perpendicular	1.1766	1.0292	13.36%
		Parallel	7.3616	2.8718	87.75%
LT R1C2	X: −169.02	45°	0.7245	1.1401	−44.58%
	Y: 50.49	Perpendicular	0.8958	0.9246	−3.16%
		Parallel	2.3002	0.4977	128.85%
RT R4C1	X: 76.08	45°	1.2436	0.7581	48.51%
	Y: 332.67	Perpendicular	1.694	0.6570	88.22%
		Parallel	5.1000	3.4188	39.47%
RT R4C2	X: 192.01	45°	4.1771	1.5755	90.45%
	Y: 331.50	Perpendicular	7.1391	0.8661	156.72
		Parallel	1.5839	0.6499	83.62%
RT R3C1	X: 77.37	45°	0.8795	0.6390	31.68%
	Y: 227.73	Perpendicular	4.9421	3.0977	45.88%
		Parallel	1.6833	0.4097	121.70%
RT R3C2	X: 194.24	45°	8.4136	0.5315	176.23%
	Y: 231.94	Perpendicular	1.1156	0.5526	67.5%
		Parallel	1.3832	0.8163	51.55%
RT R2C1	X: 77.07	45°	1.8043	1.0939	49.02%
	Y: 126.75	Perpendicular	3.5267	1.0775	106.39%
		Parallel	5.4094	1.0603	134.45%
RT R2C2	X: 195.47	45°	0.9142	0.7380	21.33%
	Y: 129.35	Perpendicular	4.1785	2.2834	58.65
		Parallel	7.7498	0.7380	165.22%
RT R1C2	X: 193.62	45°	1.2616	2.1703	−52.96%
	Y: 33.80	Perpendicular	6.2768	3.5739	54.88%

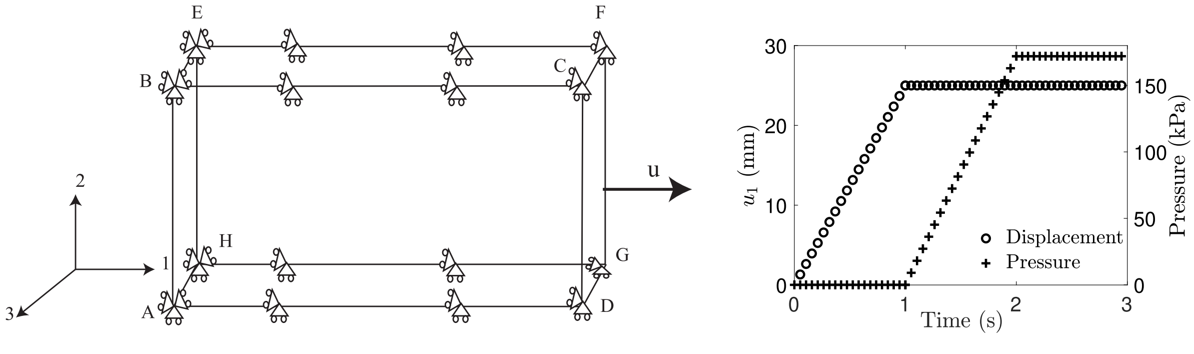

a) b)

Fig. 7. (a) Schematic of the geometry and boundary conditions for the rectangular specimen. (b) The prescribed displacement and pressure in time.

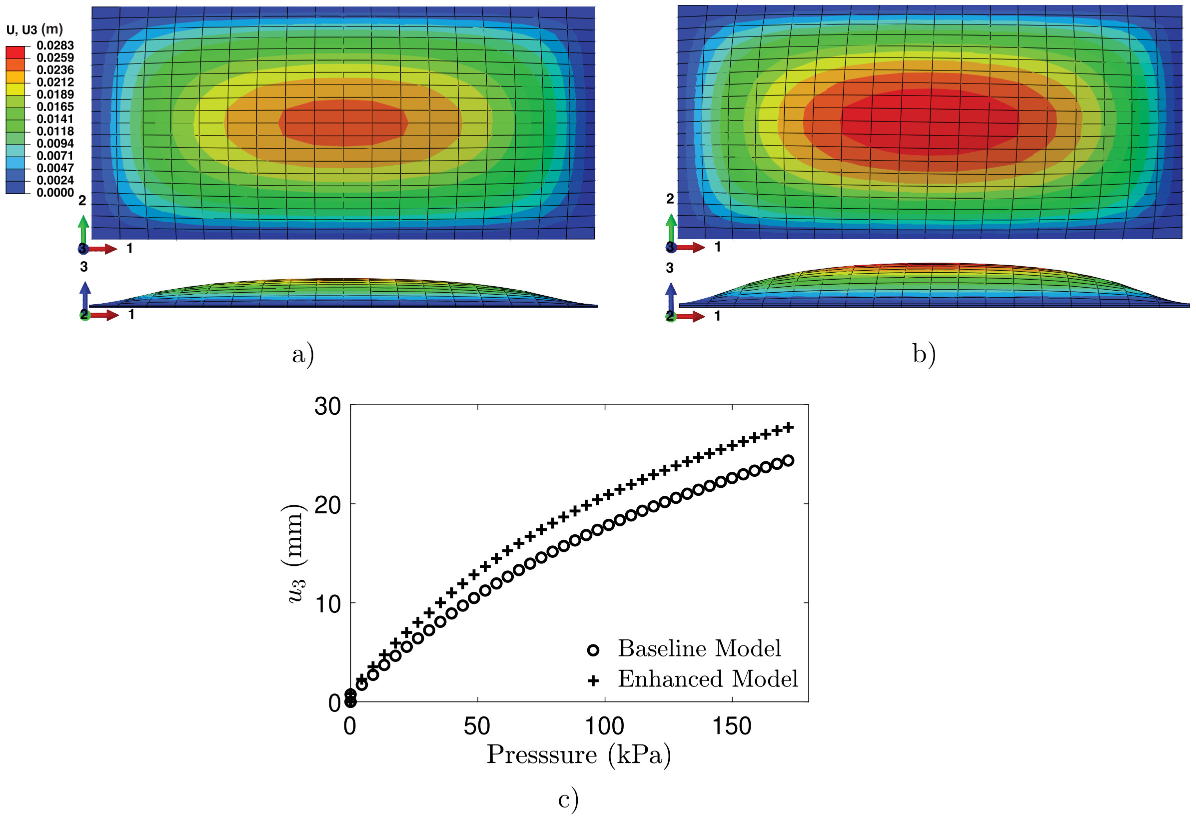

a) b) c)

Fig. 8. Contour plots of u_3 for an applied pressure of 172 kPa using (a) the baseline model, and (b) our enhanced model. (c) Comparison of the simulated displacement u_3 at the center of the rectangular strip for an applied pressure of 172 kPa.

model was demonstrated under uniaxial conditions. As shown in Fig. 6, we have demonstrated that the enhanced model captures the observed material response better than the current state of the art. And the practical relevance of this work was shown through a three-dimensional simulation using a user-defined material subroutine (VUMAT) in the commercial finite element software Abaqus/Explicit [56].

While a lot has been already accomplished to model porcine dermis, much more remains to be done. Future studies should consider the effect of aging, sex, and different anatomic location along with data from various loading regimes while characterizing the behavior of the porcine dermis.

Declaration of competing interest

The authors declare that they have no known competing financial interests or personal relationships that could have appeared to influence the work reported in this paper.

Data availability

Data will be made available on request

Acknowledgments

The authors would like to thank Midwest Research Swine, LLC for providing the material for the testing. SAC acknowledges partial support from the National Science Foundation, United States under grant numbers (CMMI-1463121) and (CMMI-1751520). SN acknowledges partial support from the National Science Foundation, United States under grant numbers (CMMI-1652409) and (CMMI-2026717). The opinions, findings, and conclusions, or recommendations expressed are those of the author(s) and do not necessarily reflect the views of the National Science Foundation. T.S. acknowledges the funding support from the Natural Sciences and Engineering Research Council (Discovery grant RGPIN-2021-02643).

References

[1] J.-L. De Rigal, In vivo measurement of the stratum corneum elasticity, Bioeng. Skin (ISSN: 0266-3082) (1985).

[2] J. Hochberg, K.M. Meyer, M.D. Marion, Suture choice and other methods of skin closure, Surg. Clin. N. Am. (ISSN: 0039-6109) 89 (3) (2009) 627—641, http://dx.doi.org/10.1016/j.suc.2009.03.001.

[3] G.W. Wood, M.B. Panzer, C.R. Bass, B.S. Myers, Viscoelastic properties of hybrid III head skin, SAE Int. J. Mater. Manuf. 3 (1) (2010) 186–193, URL http://www.jstor.org/stable/26282897.

[4] H. Joodaki, J. Forman, A. Forghani, B. Overby, R. Kent, J. Crandall, B. Beahlen, M. Beebe, O. Bostrom, Comparison of kinematic behaviour of a first generation obese dummy and obese PMHS in frontal sled tests, in: 2015 IRCOBI Conference Proceedings - International Research Council on the Biomechanics of Injury, 2015, pp. 454–466.

[5] A. Rastegarpour, M. Cheung, M. Vardhan, M.M. Ibrahim, C.E. Butler, H. Levinson, Surgical mesh for ventral incisional hernia repairs: Understanding mesh design, Plast. Surg. 24 (1) (2016) 41–50, http://dx.doi.org/10.1177/229255031602400110.

[6] H. Logan Ellis, O. Asaolu, V. Nebo, A. Kasem, Biological and synthetic mesh use in breast reconstructive surgery: A literature review, World J. Surg. Oncol. (ISSN: 14777819) 14 (1) (2016) 1–9, http://dx.doi.org/10.1186/s12957-016-0874-9.

[7] J.W.Y. Jor, P.M.F. Nielsen, M.P. Nash, P.J. Hunter, Modelling collagen fibre orientation in porcine skin based upon confocal laser scanning microscopy, Skin Res. Technol. 17 (2) (2011) 149–159, http://dx.doi.org/10.1111/j.1600-0846.2011.00471.x, URL https://onlinelibrary.wiley.com/doi/abs/10.1111/j.1600-0846.2011.00471.x.

[8] J.M. Benítez, F.J. Montáns, The mechanical behavior of skin: Structures and models for the finite element analysis, Comput. Struct. (ISSN: 00457949) 190 (2017) 75–107, http://dx.doi.org/10.1016/j.compstruc.2017.05.003.

[9] G. Wilkes, I. Brown, R. Wildnauer, The biomechanical properties of skin, CRC Crit. Rev. Bioeng. (ISSN: 0045-642X) 1 (4) (1973) 453—495, URL http://europepmc.org/abstract/MED/4581809.

[10] J. Craik, I. Mcneil, 14 - Histological Studies of stressed skin, in: R. Kenedi (Ed.), Biomechanics and Related Bio-Engineering Topics, Pergamon Press, Oxford, ISBN: 978-1-4831-6701-5, 1965, pp. 159–164, http://dx.doi.org/10.1016/B978-1-4831-6701-5.50023-1, URL https://www.sciencedirect.com/science/article/pii/B9781483167015500231.

[11] J.W. Jor, M.P. Nash, P.M. Nielsen, P.J. Hunter, Estimating material parameters of a structurally based constitutive relation for skin mechanics, Biomech. Model. Mechanobiol. (ISSN: 16177959) 10 (5) (2011) 767–778, http://dx.doi.org/10.1007/s10237-010-0272-0.

[12] A.N. Annaidh, K. Bruyère, M. Destrade, M.D. Gilchrist, C. Maurini, M. Otténio, G. Saccomandi, Automated estimation of collagen fibre dispersion in the dermis and its contribution to the anisotropic behaviour of skin, Ann. Biomed. Eng. (ISSN: 00906964) 40 (8) (2012) 1666–1678, http://dx.doi.org/10.1007/s10439-012-0542-3.

[13] H. Joodaki, M.B. Panzer, Skin mechanical properties and modeling: A review, Proc. Inst. Mech. Eng. H: J. Eng. Med. 232 (4) (2018) 323–343, http://dx.doi.org/10.1177/0954411918759801, URL https://doi.org/10.1177/0954411918759801, PMID: 29506427.

[14] W. Krasny, C. Morin, H. Magoariec, S. Avril, A comprehensive study of layer-specific morphological changes in the microstructure of carotid arteries under uniaxial load, Acta Biomater. 57 (2017) 342–351.

[15] M.G. Dunn, F.H. Silver, Viscoelastic behavior of human connective tissues: Relative contribution of viscous and elastic components, Connect. Tissue Res. (ISSN: 03008207) 12 (1) (1983) 59–70, http://dx.doi.org/10.3109/03008208309005612.

[16] C. Jacquemoud, K. Bruyere-Garnier, M. Coret, Methodology to determine failure characteristics of planar soft tissues using a dynamic tensile test, J. Biomech. (ISSN: 00219290) 40 (2) (2007) 468–475, http://dx.doi.org/10.1016/j.jbiomech.2005.12.010.

[17] M. Ottenio, D. Tran, A. Ní Annaidh, M.D. Gilchrist, K. Bruyère, Strain rate and anisotropy effects on the tensile failure characteristics of human skin, J. Mech. Behav. Biomed. Mater. (ISSN: 18780180) 41 (2015) 241–250, http://dx.doi.org/10.1016/j.jmbbm.2014.10.006.

[18] D. Pond, A.T. McBride, L.M. Davids, B.D. Reddy, G. Limbert, Microstructurally-based constitutive modelling of the skin – Linking intrinsic ageing to microstructural parameters, J. Theoret. Biol. (ISSN: 10958541) 444 (2018) 108–123, http://dx.doi.org/10.1016/j.jtbi.2018.01.014.

[19] M.S. Sacks, A method for planar biaxial mechanical testing that includes in-plane shear, J. Biomech. Eng. (ISSN: 15288951) 121 (5) (1999) 551–555, http://dx.doi.org/10.1115/1.2835086.

[20] A.A.K. Yousefi, M.A. Nazari, P. Perrier, M.S. Panahi, Y. Payan, A visco-hyperelastic constitutive model and its application in bovine tongue tissue, J. Biomech. (ISSN: 18732380) 71 (2018) 190–198, http://dx.doi.org/10.1016/j.jbiomech.2018.02.008.

[21] R.C. Haut, The effects of orientation and location on the strength of dorsal rat skin in high and low speed tensile failure experiments, J. Biomech. Eng. (ISSN: 15288951) 111 (2) (1989) 136–140, http://dx.doi.org/10.1115/1.3168354.

[22] O.A. Shergold, N.A. Fleck, D. Radford, The uniaxial stress versus strain response of pig skin and silicone rubber at low and high strain rates, Int. J. Impact Eng. (ISSN: 0734743X) 32 (9) (2006) 1384–1402, http://dx.doi.org/10.1016/j.ijimpeng.2004.11.010.

[23] B. Zhou, F. Xu, C.Q. Chen, T.J. Lu, Strain rate sensitivity of skin tissue under thermomechanical loading, Phil. Trans. R. Soc. A (ISSN: 1364503X) 368 (1912) (2010) 679–690, http://dx.doi.org/10.1098/rsta.2009.0238.

[24] J. Lim, J. Hong, W.W. Chen, T. Weerasooriya, Mechanical response of pig skin under dynamic tensile loading, Int. J. Impact Eng. (ISSN: 0734743X) 38 (2–3) (2011) 130–135, http://dx.doi.org/10.1016/j.ijimpeng.2010.09.003.

[25] B. Zhang, S.A. Chester, S.P.V. Nadimpalli, J.T. Suriano, D.P. Theis, S.C. Lieber, Mechanical characterization of porcine skin starting material, J. Eng. Sci. Med. Diagn. Ther. (ISSN: 2572-7958) 4 (4) (2021) http://dx.doi.org/10.1115/1.4051563, 041002.

[26] S.D. Łagan, A. Liber-Kneć, Experimental testing and constitutive modeling of the mechanical properties of the swine skin tissue, Acta Bioeng. Biomech. 19 (2) (2017) 93–102.

[27] A. Pissarenko, W. Yang, H. Quan, K.A. Brown, A. Williams, W.G. Proud, M.A. Meyers, Tensile behavior and structural characterization of pig dermis, Acta Biomater. 86 (2019) 77–95.

[28] S. Jaiswal, R. Hannineh, S. Nadimpalli, S. Lieber, S.A. Chester, Characterization and modeling of the in-plane collagen fiber distribution in the porcine dermis, Med. Eng. Phycis (ISSN: 1350-4533) 115 (2023) 103973, http://dx.doi.org/10.1016/j.medengphy.2023.103973.

[29] R.N. Vaishnav, J.T. Young, J.S. Janicki, D.J. Patel, Nonlinear anisotropic elastic properties of the canine aorta, Biophys. J. (ISSN: 00063495) 12 (8) (1972) 1008–1027, http://dx.doi.org/10.1016/S0006-3495(72)86140-X.

[30] Y. Fung, K. Fronek, P. Patitucci, Pseudoelasticity of arteries and the choice of its mathematical expression, Am. J. Physiol.-Heart Circul. Physiol. 237 (5) (1979) H620–H631.

[31] K. Takamizawa, K. Hayashi, Strain energy density function and uniform strain hypothesis for arterial mechanics, J. Biomech. (ISSN: 0021-9290) 20 (1) (1987) 7–17, http://dx.doi.org/10.1016/0021-9290(87)90262-4, URL http://www.sciencedirect.com/science/article/pii/0021929087902624.

[32] G.A. Holzapfel, T.C. Gasser, R.W. Ogden, A new constitutive framework for arterial wall mechanics and a comparative study of material models, J. Elasticity (ISSN: 03743535) 61 (1–3) (2000) 1–48, http://dx.doi.org/10.1023/A:1010835316564.

[33] T.C. Gasser, R.W. Ogden, G.A. Holzapfel, Hyperelastic modelling of arterial layers with distributed collagen fibre orientations, J. R. Soc. Interface 3 (6) (2006) 15–35.

[34] G.A. Holzapfel, R.W. Ogden, Constitutive modelling of arteries, Proc. R. Soc. A 466 (2118) (2010) 1551–1597.

[35] Y. Wang, S. Son, S.M. Swartz, N.C. Goulbourne, A mixed von mises distribution for modeling soft biological tissues with two distributed fiber properties, Int. J. Solids Struct. (ISSN: 00207683) 49 (21) (2012) 2914–2923, http://dx.doi.org/10.1016/j.ijsolstr.2012.04.004.

[36] G.A. Holzapfel, J.A. Niestrawska, R.W. Ogden, A.J. Reinisch, A.J. Schriefl, Modelling non-symmetric collagen fibre dispersion in arterial walls, J. R. Soc. Interface 12 (106) (2015) 20150188.

[37] W. Li, X.Y. Luo, An invariant-based damage model for human and animal skins, Ann. Biomed. Eng. 44 (10) (2016) 3109–3122.

[38] M. Bajuri, H. Isaksson, P. Eliasson, M.S. Thompson, A hyperelastic fibre-reinforced continuum model of healing tendons with distributed collagen fibre orientations, Biomech. Model. Mechanobiol. 15 (6) (2016) 1457–1466.

[39] H.-C. Han, Effects of material non-symmetry on the mechanical behavior of arterial wall, J. Mech. Behav. Biomed. Mater. 129 (2022) 105157.

[40] T.P. Sullivan, W.H. Eaglstein, S.C. Davis, P. Mertz, The pig as a model for human wound healing, Wound Repair Regener. 9 (2) (2001) 66–76.

[41] B. Godin, E. Touitou, Transdermal skin delivery: predictions for humans from in vivo, ex vivo and animal models, Adv. Drug Deliv. Rev. 59 (11) (2007) 1152–1161.

[42] M. Żak, P. Kuropka, M. Kobielarz, A. Dudek, K. Kaleta-Kuratewicz, S. Szotek, Determination of the mechanical properties of the skin of pig foetuses with respect to its structure, Acta Bioeng. Biomech. 13 (2) (2011) 37–43.

[43] M.M. Swindle, A. Makin, A.J. Herron, F.J. Clubb, K.S. Frazier, Swine as models in biomedical research and toxicology testing, Vet. Pathol. (ISSN: 15442217) 49 (2) (2012) 344–356, http://dx.doi.org/10.1177/0300985811402846.

[44] T. Foutz, E. Stone, C. Abrams Jr., Effects of freezing on mechanical properties of rat skin, Am. J. Vet. Res. 53 (5) (1992) 788–792.

[45] S. Ranamukhaarachchi, S. Lehnert, S. Ranamukhaarachchi, L. Sprenger, T. Schneider, I. Mansoor, K. Rai, U. Häfeli, B. Stoeber, A micromechanical comparison of human and porcine skin before and after preservation by freezing for medical device development, Sci. Rep. 6 (1) (2016) 1–9.

[46] J.O.V. Delgadillo, S. Delorme, R. El-Ayoubi, R. DiRaddo, S.G. Hatzikiriakos, et al., Effect of freezing on the passive mechanical properties of arterial samples, J. Biomed. Sci. Eng. 3 (07) (2010) 645.

[47] R. Rezakhaniha, A. Agianniotis, J.T. Schrauwen, A. Griffa, D. Sage, C.V. Bouten, F.N. Van De Vosse, M. Unser, N. Stergiopulos, Experimental investigation of collagen waviness and orientation in the arterial adventitia using confocal laser scanning microscopy, Biomech. Model. Mechanobiol. (ISSN: 16177959) 11 (3–4) (2012) 461–473, http://dx.doi.org/10.1007/s10237-011-0325-z.

[48] D. Lecompte, A. Smits, S. Bossuyt, H. Sol, J. Vantomme, D. Van Hemelrijck, A. Habraken, Quality assessment of speckle patterns for digital image correlation, Opt. Lasers Eng. (ISSN: 0143-8166) 44 (11) (2006) 1132–1145, http://dx.doi.org/10.1016/j.optlaseng.2005.10.004, URL https://www.sciencedirect.com/science/article/pii/S0143816605001727.

[49] S. Wang, S.A. Chester, Experimental characterization and continuum modeling of inelasticity in filled rubber-like materials, Int. J. Solids Struct. 136 (2018) 125–136.

[50] K. Alkhoury, N. Bosnjak, Y. Wang, H. Lee, S. Nadimpalli, S.A. Chester, Experiments and modeling of the thermo-mechanically coupled behavior of VHB, Int. J. Solids Struct. 242 (2022) 111523.

[51] ASTM D638, ASTM D638-14. Standard Test Method for Tensile Properties of Plastics, ASTM International, West Conshohocken, PA, 2014.

[52] J. Lim, J. Hong, W.W. Chen, T. Weerasooriya, Mechanical response of pig skin under dynamic tensile loading, Int. J. Impact Eng. 38 (2–3) (2011) 130–135.

[53] R.W. Ogden, Anisotropy and nonlinear elasticity in arterial wall mechanics, in: Biomechanical Modelling At the Molecular, Cellular and Tissue Levels, Springer, 2009, pp. 179–258.

[54] D.H. Cortes, S.P. Lake, J.A. Kadlowec, L.J. Soslowsky, D.M. Elliott, Characterizing the mechanical contribution of fiber angular distribution in connective tissue: comparison of two modeling approaches, Biomech. Model. Mechanobiol. 9 (5) (2010) 651–658.

[55] Y. Bai, N.J. Kaiser, K.L. Coulombe, V. Srivastava, A continuum model and simulations for large deformation of anisotropic fiber–matrix composites for cardiac tissue engineering, J. Mech. Behav. Biomed. Mater. 121 (2021) 104627.

[56] Abaqus/Explicit, Abaqus Reference Manuals, Dassault Systemes Simulia, Providence, RI, 2019.